

Identification of Mechanical Models for Golf Ball Materials Using a Viscoelastic Split Hopkinson Pressure Bar

Takayuki Tamaogi¹ · Yuji Sogabe² · Zhiqiang Wu² · Takashi Yokoyama³

Received: 20 January 2017 / Accepted: 23 March 2017 / Published online: 10 April 2017
© Society for Experimental Mechanics, Inc 2017

Abstract A viscoelastic (polymeric) split Hopkinson pressure bar (SHPB) was used as a means of determining the dynamic characteristics of low-impedance or soft materials. The present viscoelastic SHPB consists of polymethyl methacrylate (PMMA) bars to account for the impedance mismatch between test specimens and metallic bars. Wave propagation analysis of strain pulses in a PMMA bar was executed in the frequency domain to identify its mechanical model using elementary one-dimensional wave theory. The SHPB made of PMMA bars was applied to evaluate the high strain rate compressive properties of core and cover materials for a two-piece golf ball within nearly 0.10 strain. Complex compliances of polybutadiene rubber (core) and ionomer resin (cover) specimens, which are the ratios of the strain to stress in the frequency domain, were determined to identify the respective mechanical models. To validate the accuracy of the mechanical models for golf ball materials, finite element investigations on axial collisions between the golf ball and a long elastic bar were conducted for comparison with measured contact force histories. It is demonstrated that three-element solid models can describe the dynamic behavior of both the core and cover materials within a given frequency range. The limitations of the models are also discussed.

Keywords Complex compliance · FE analysis · Golf ball impact · Low-impedance material · Mechanical model · Viscoelastic Hopkinson pressure bar

Introduction

The use of polymeric materials has been increasing in various industries such as automotive, sports, and electronic industries because of their excellent impact resistance and energy-absorbing capability. Precise knowledge of their dynamic behavior is needed to further widen the applicability of polymeric materials. The split Hopkinson pressure bar (SHPB), originally developed by Kolsky, [1] has been widely recognized as one of the most reliable experimental methods for measuring the high strain rate properties of engineering materials. Nevertheless, a conventional SHPB made from metallic bars has great difficulties in accurately characterizing low-impedance materials because of a larger impedance mismatch between specimen materials and metallic bars. To be more specific, a transmitted strain signal in a metallic output bar is so low that it is very difficult to precisely characterize their high strain rate stress–strain behavior. Recently, numerous researchers have been concerned with SHPB techniques for evaluating the dynamic properties of low-impedance or soft materials such as polymers, polymeric foams, rubbers, and biological tissues. For this purpose, they replaced input and output metallic bars with corresponding viscoelastic bars to reduce the impedance mismatch between specimens and metallic bars. A specific problem usually arises when input and output bars made of polymeric materials are used. Since such materials exhibit viscoelastic effects, we need to take into account the attenuation and dispersion of strain waves propagating in polymeric bars. A crucial point for accurately

✉ Takayuki Tamaogi
tamaogi@mec.niihama-nct.ac.jp

¹ Niihama College, National Institute of Technology, 7-1 Yakumo-cho, Niihama, Ehime 792-8580, Japan

² Ehime University, Matsuyama, Ehime 790-8577, Japan

³ Okayama University of Science, Okayama 700-0005, Japan

determining the dynamic properties of specimens is to correct the waveforms of strain pulses traveling along polymeric bars. Wang et al. [2] first developed a viscoelastic SHPB technique. They incorporated the viscoelastic effects into the one-dimensional wave equation and used a simple three-element model (or a standard linear solid model). Aleyaasin and Harrigan [3] recently used the same model to incorporate the effect of lateral inertia in a viscoelastic equivalent to the Love equation. Zhao and Garry [4] generalized the Pochhammer-Chree equation for elastic bars to viscoelastic bars, and used a nine-parameter model for PMMA (polymethyl methacrylate) bars. These parameters were determined from experimental strain histories through an inverse analysis. Sogabe et al. [5] proposed an alternative viscoelastic SHPB method, and thereby identified a mechanical model of ABS resin, in which corrections of the waveforms were conducted in the frequency domain using Fourier transforms. Zhao et al. [6] analyzed the use and modeling of polymeric pressure bars in the SHPB. Subsequently, Zhao and his coworker applied a viscoelastic SHPB to characterize the dynamic behavior of polymeric foams [7], polymer matrix composite plates [8], and aluminum honeycombs [9]. Zhao and Gary [10], and Bacon [11, 12] studied wave dispersion and attenuation for a viscoelastic SHPB method. Bacon and Brun [13] presented a polymeric SHPB method for predicting wave propagation in elastic and viscoelastic non-uniform bars. Sawas et al. [14] developed a detailed procedure for correcting the viscoelastic wave and calculating the stress–strain data for two different compliant materials. Cheng et al. [15] devised a viscoelastic SHPB, in which corrections of the wave dispersion and attenuation were made using spectral analysis. Bussac et al. [16] used analytical models to quantify the errors associated with predicting forces and displacements in bars from strain and velocity records at other positions in the bar. Casem et al. [17] investigated a wave separation technique that is applicable to viscoelastic wave propagation. Subsequently, Casem et al. [18] discussed a polycarbonate SHPB equipped with electromagnetic velocity gages and applied it to test low-density foams. Mousavi et al. [19] discussed the accuracy of the compression modulus of a polypropylene (PP) specimen determined using a non-equilibrium viscoelastic SHPB. Liu and Subhash [20] presented a new approach to characterize the viscoelastic behavior of polymer (or cast acrylic) bars in the time domain using wave propagation phenomena. Doman et al. [21] and Quellet et al. [22] applied a viscoelastic SHPB to determine the high strain rate compressive response of polyurethane rubber and three types of polymeric foams, respectively. Bussac et al. [23] reported an analytical model for the strain histories resulting from the viscoelastic impact of a cylindrical striker and a long cylindrical bar. Salisbury and Cronin [24] measured the high strain

rate compressive properties of ballistic gelatin (used as a soft tissue simulant) using two viscoelastic SHPBs. Ahonsi et al. [25] investigated two different techniques for accurately determining the propagation coefficient of longitudinal stress waves in PMMA bars. Butt and Xue [26] also determined the wave propagation coefficient from longitudinal strain waves in PMMA bars. Harrigan et al. [27] conducted finite element simulations for verifying the accuracy of the test data from a viscoelastic SHPB. Butt et al. [28] proposed a parametric identification method for viscoelastic parameters of PMMA using the wave propagation test data and identified five parameters of a generalized Maxwell model. Johnson et al. [29] and Itrausquín et al. [30] characterized the dynamic behavior of polyurea and closed-cell aluminum foams using PMMA bars, respectively, with the help of Bacon's method [11].

In the present work, a viscoelastic SHPB made of PMMA bars was developed to characterize the dynamic behavior of low-impedance materials. The viscoelastic SHPB technique was applied to identify mechanical models for two-piece golf ball materials under the assumption that the geometric dispersion (or three-dimensional effects) can be neglected. The validity of three-element solid models identified was verified by FE analysis and impact tests for axial collision between a golf ball and a long elastic bar.

Viscoelastic SHPB Technique

Theory of Wave Propagation in a Viscoelastic Bar

We will consider the elementary one-dimensional theory of a longitudinal wave in a cylindrical bar. The one-dimensional equation of longitudinal wave motion is written as

$$\frac{\partial^2 \sigma}{\partial x^2} = \rho \frac{\partial^2 \epsilon}{\partial t^2} \quad (1)$$

where σ and ϵ denote the axial stress and strain, respectively; ρ is the mass density of the bar; x is the coordinate along the bar axis, and t is the time. The constitutive equation for a linear viscoelastic solid is expressed in a generalized form as [31]

$$P(D)\sigma = Q(D)\epsilon \quad (2)$$

where $D = \partial/\partial t$ indicates a differential operator; $P(D)$ and $Q(D)$ are polynomials in terms of D . The Fourier transform of a function $f(t)$ defined in terms of time t is given by

$$\bar{f}(\omega) = \int_{-\infty}^{\infty} f(t) \cdot \exp(-i\omega t) dt, \quad (3)$$

where ω is an angular frequency. Applying the Fourier transform to Eqs. (1) and (2) leads to

$$\frac{d^2 \bar{\sigma}(\omega)}{dx^2} = (i\omega)^2 \bar{\epsilon}(\omega) = -\rho\omega^2 \bar{\epsilon}(\omega), \quad (4)$$

$$P(i\omega)\bar{\sigma}(\omega) = Q(i\omega)\bar{\epsilon}(\omega). \quad (5)$$

Substitution of Eq. (5) into Eq. (4) yields the Fourier transformed wave equation:

$$\left\{ \frac{d^2}{dx^2} + \rho\omega^2 J(\omega) \right\} \bar{\epsilon}(\omega) = 0. \quad (6)$$

where $J(\omega)$ is a complex compliance defined in terms of $P(i\omega)$ and $Q(i\omega)$ or $\bar{\sigma}(\omega)$ and $\bar{\epsilon}(\omega)$ as

$$J(\omega) = J_1(\omega) - iJ_2(\omega) = \frac{P(i\omega)}{Q(i\omega)} = \frac{\bar{\sigma}(\omega)}{\bar{\epsilon}(\omega)}. \quad (7)$$

The complex compliance $J(\omega)$ represents a frequency response of the linear viscoelastic material; its real part $J_1(\omega)$ indicates a storage compliance and its imaginary part $J_2(\omega)$ indicates a loss compliance. The solution to Eq. (6) for a semi-infinite bar ($0 \leq x < \infty$) is given by

$$\bar{\epsilon}(x, \omega) = \bar{\epsilon}(0, \omega) \cdot \exp[-\{\alpha(\omega) + ik(\omega)\}x], \quad (8)$$

where $\bar{\epsilon}(0, \omega)$ is the Fourier transform of $\epsilon(0, t)$ corresponding to a strain wave propagating in the positive x -direction; $\alpha(\omega)$ and $k(\omega)$ are the attenuation (or damping) coefficient and the wavenumber, respectively, which are related to $J_1(\omega)$ and $J_2(\omega)$ by

$$\left. \begin{aligned} k(\omega)^2 - \alpha(\omega)^2 &= \rho\omega^2 J_1(\omega) \\ 2\alpha(\omega) \cdot k(\omega) &= \rho\omega^2 J_2(\omega) \end{aligned} \right\}, \quad (9)$$

where $\alpha(\omega)$ quantifies the reduction in magnitude of a propagating wave, whereas $k(\omega) = [\omega/C(\omega)]$ is related to the phase velocity $C(\omega)$ and quantifies the dispersion of waves with different frequencies.

Correction of Waveforms in Viscoelastic SHPB

Figure 1 shows a schematic of the present SHPB setup consisting of an input bar, an output bar, and a striker bar of PMMA. A cylindrical specimen is sandwiched between input and output bars. Strain gages ① and ② are placed on the input and output bars, respectively. When the input bar is impacted by a striker bar launched with compressed air through a gun barrel, an incident strain pulse $\epsilon_i^\circ(t)$ is generated in the input bar and propagates toward the specimen. Part of this is reflected at the bar/specimen interface A. Its

remaining part propagates through the specimen and into the output bar. The incident strain pulse and reflected strain pulse $\epsilon_r^\circ(t)$ are measured with strain gage ① and the transmitted strain pulse $\epsilon_t^\circ(t)$ is recorded with strain gage ②. Let $\bar{\epsilon}_i^\circ(\omega)$, $\bar{\epsilon}_r^\circ(\omega)$, and $\bar{\epsilon}_t^\circ(\omega)$ be the Fourier transforms of the three measured strain pulses. From Eq. (8), we can derive the following solutions for correcting the respective strain pulses to be the waveforms at interfaces A and B:

$$\bar{\epsilon}_i^A(\omega) = \bar{\epsilon}_i^\circ(\omega) \cdot \exp[+\{\alpha(\omega) + ik(\omega)\}l_1] \quad (10)$$

$$\bar{\epsilon}_r^A(\omega) = \bar{\epsilon}_r^\circ(\omega) \cdot \exp[+\{\alpha(\omega) + ik(\omega)\}l_1] \quad (11)$$

$$\bar{\epsilon}_t^B(\omega) = \bar{\epsilon}_t^\circ(\omega) \cdot \exp[+\{\alpha(\omega) + ik(\omega)\}l_2] \quad (12)$$

where l_1 indicates the distance between strain gage ① and interface A; l_2 denotes the distance between strain gage ② and interface B. Note that the signs in the exponential terms of Eqs. (11) and (12) must be positive (+) because the reflected and transmitted strain pulses should be corrected in the reverse directions of their wave propagation. In this way, using Eqs. (10) to (12), the incident and reflected strain pulses can be corrected to be those at interface A, and the transmitted one can be corrected to be that at interface B. We can obtain the corrected waveforms of three strain pulses in the time domain by applying the inverse Fourier transform to Eqs. (10) to (12), where the inverse Fourier transform of $\bar{f}(\omega)$ is defined by

$$f(t) = \frac{1}{2\pi} \int_{-\infty}^{\infty} \bar{f}(\omega) \cdot \exp(i\omega t) d\omega. \quad (13)$$

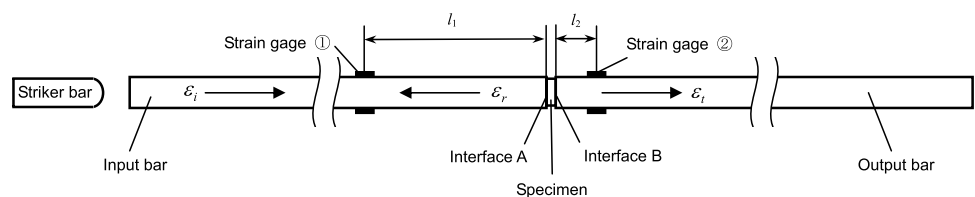
Consequently, we can determine $\epsilon_i^A(t)$, $\epsilon_r^A(t)$, and $\epsilon_t^B(t)$ at both interfaces A and B.

Viscoelastic SHPB Testing

Preparation of Test Materials and Specimen Geometry

Two different low-impedance materials were chosen in this work. A polybutadiene rubber and an ionomer resin, which were used as the core and cover materials of a two-piece golf ball (Windy 384 KASCO, Japan), were tested to examine their dynamic properties. The materials were molded into cylindrical specimens under the same conditions

Fig. 1 Schematic of SHPB setup made with PMMA bars



as used in manufacturing the golf balls, and their dimensions are listed in Table 1. The slenderness ratio l/d given in Table 1 is much smaller than the values of $l/d=0.5$ – 1 [32] usually adopted in conventional SHPB tests. This is mainly because of difficulties in achieving dynamic stress equilibrium within the low-impedance specimens. Similar specimens with smaller slenderness ratios l/d that were far less than 0.5 were also used in the modified SHPB testing of RTV630 silicone rubber [33] and in the conventional SHPB testing of two polymers [34].

Stress, Strain Rate, and Strain of Specimen

The viscoelastic SHPB tests were conducted at room temperature of 20–25 °C using the same measurement system as used in the wave propagation experiments (see Fig. 16). The viscoelastic response of PMMA bars is sensitive to ambient temperatures, but our preliminary tests indicated that their viscoelastic properties remain almost unchanged in the above temperature range. The dimensions of the input/output bars and the striker bar are listed in Table 2, including the strain gage's locations from interfaces A and B. To minimize frictional effects, a thin layer of petroleum jelly was applied between the specimen ends and the input/output bars, but a pulse shaper was not used in this work. Figure 2 presents typical strain gage records from the viscoelastic SHPB test on the polybutadiene rubber (core material) specimen with a 12 mm diameter and a 4 mm length. The top trace gives the incident and reflected strain

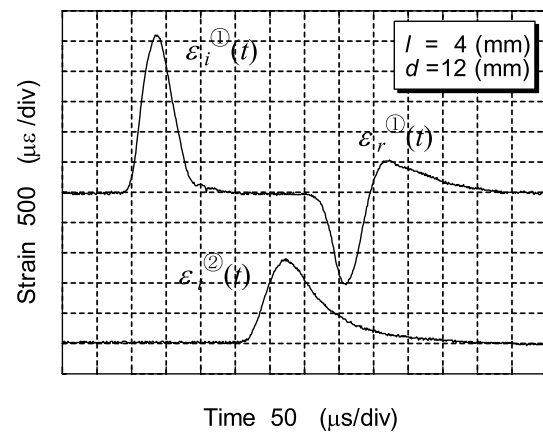


Fig. 2 Typical strain gage records from viscoelastic SHPB test on polybutadiene rubber specimen (Note: compression is upward and tension is downward)

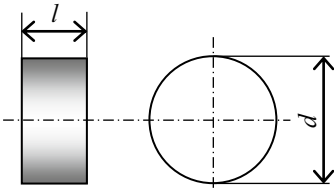
pulses ($\varepsilon_i^{\odot}(t)$ and $\varepsilon_r^{\odot}(t)$) and the bottom trace gives the transmitted strain pulse ($\varepsilon_t^{\odot}(t)$). The strain gage signals were recorded at a sampling rate of 1 MHz. Note that the durations of the reflected and transmitted strain pulses are much longer than that of the incident strain pulse ($\approx 170 \mu\text{s}$). Figure 3a shows the three corrected strain pulses, $\varepsilon_i^A(t)$, $\varepsilon_r^A(t)$, and $\varepsilon_t^B(t)$, calculated from the inverse Fourier transforms. A close look at Fig. 3b suggests that the relation $\varepsilon_i^A(t) - \{-\varepsilon_r^A(t)\} = \varepsilon_t^B(t)$ holds. By applying the Fourier transform to the three strain waves, we can evaluate the front stress $\bar{\sigma}^A(\omega)$ at interface A and the back stress $\bar{\sigma}^B(\omega)$ at interface B in the frequency domain:

$$\bar{\sigma}^A(\omega) = \frac{1}{J(\omega)} \{ \bar{\varepsilon}_i^A(\omega) + \bar{\varepsilon}_r^A(\omega) \}, \quad (14)$$

$$\bar{\sigma}^B(\omega) = \frac{\bar{\varepsilon}_t^B(\omega)}{J(\omega)}, \quad (15)$$

where $J(\omega)$ of PMMA is given by Eq. (A3). The stresses $\sigma^A(t)$ and $\sigma^B(t)$ in the time domain can be derived by applying the inverse Fourier transform to Eqs. (14) and (15). Figure 4 gives the compressive stress histories applied at both ends of the specimen, verifying that dynamic stress equilibrium within the specimen was achieved. Preliminary tests revealed that dynamic stress equilibrium was not achieved either in the polybutadiene rubber specimen or in the ionomer resin specimen for a length longer than 6 mm. This is because the wave velocities (≈ 240 – 570 m/s) in the golf ball materials with a lower mechanical impedance was by far lower than those in metallic materials. Therefore, we must use specimens with smaller slenderness ratios in the viscoelastic SHPB tests. The stress $\sigma_s(t)$, strain rate $\dot{\varepsilon}_s(t)$, and strain $\varepsilon_s(t)$ of the specimen were obtained from a three-wave stress analysis of the SHPB test [35] as

Table 1 Shape and dimensions of compression specimens



Material	Length l (mm)	Diameter d (mm)	Slenderness ratios l/d
Polybutadiene rubber (Core of Golf ball)	4.0, (6.0) ^a	12.0	1/3, (1/2) ^a
Ionomer resin (Cover of golf ball)			

^aDynamic stress equilibrium did not hold within compression specimens with slenderness ratio of 1/2

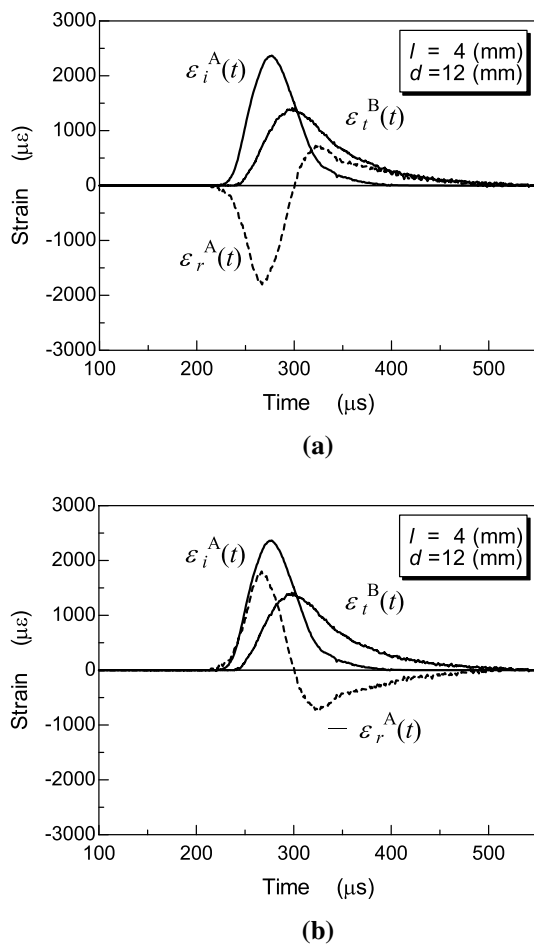


Fig. 3 Three typical strain pulses from polybutadiene rubber specimen. **a** Three corrected strain pulses, **b** Three time-shifted strain pulses including inverted reflected strain pulse

$$\sigma_s(t) = \frac{EA\{\epsilon_i^A(t) + \epsilon_r^A(t) + \epsilon_t^B(t)\}}{2A_s} \quad (16)$$

$$\dot{\epsilon}_s(t) = \sqrt{\frac{E}{\rho}} \cdot \frac{1}{l_s} \{\epsilon_i^A(t) - \epsilon_r^A(t) - \epsilon_t^B(t)\} \quad (17)$$

$$\epsilon_s(t) = \sqrt{\frac{E}{\rho}} \cdot \frac{1}{l_s} \int_0^t \{\epsilon_i^A(t) - \epsilon_r^A(t) - \epsilon_t^B(t)\} dt \quad (18)$$

where E , ρ , and A are the Young's modulus, the mass density, and the cross-sectional area of the input and output elastic bars; l_s and A_s are the length and the cross-sectional area of the specimen. Under the assumption of force equilibrium across the specimen, we can simplify Eqs. (16) to (18) as

$$\sigma_s(t) = \frac{EA\epsilon_t^B(t)}{A_s} \quad (19)$$

$$\dot{\epsilon}_s(t) = \sqrt{\frac{E}{\rho}} \cdot \frac{2}{l_s} \{\epsilon_i^A(t) - \epsilon_t^B(t)\} \quad (20)$$

$$\epsilon_s(t) = \sqrt{\frac{E}{\rho}} \cdot \frac{2}{l_s} \int_0^t \{\epsilon_i^A(t) - \epsilon_t^B(t)\} dt \quad (21)$$

By applying the Fourier transform to Eqs. (19) to (21) and replacing Young's modulus E with a reciprocal of the complex compliance $J(\omega)$ of the input and output bars of PMMA, we can obtain the stress, strain rate and strain of the specimen in the frequency domain:

$$\bar{\sigma}_s(\omega) = \frac{A\bar{\epsilon}_t^B(\omega)}{A_s J(\omega)}, \quad (22)$$

$$\bar{\dot{\epsilon}}_s(\omega) = \sqrt{\frac{1}{\rho J(\omega)}} \cdot \frac{2}{l_s} \{\bar{\epsilon}_i^A(\omega) - \bar{\epsilon}_t^B(\omega)\}, \quad (23)$$

$$\begin{aligned} \bar{\epsilon}_s(\omega) &= \sqrt{-\frac{1}{\rho \omega^2 J(\omega)}} \cdot \frac{2}{l_s} \{\bar{\epsilon}_i^A(\omega) - \bar{\epsilon}_t^B(\omega)\} \\ &= \frac{2}{\{\alpha(\omega) + ik(\omega)\} l_s} \{\bar{\epsilon}_i^A(\omega) - \bar{\epsilon}_t^B(\omega)\}. \end{aligned} \quad (24)$$

Note that Eq. (24) can be derived using Eqs. (7) and (9). $J(\omega)$, $\alpha(\omega)$, and $k(\omega)$ of PMMA were determined using Eq. (A3). By applying the inverse Fourier transform to Eqs. (22) to (24), we have the stress, strain rate, and strain of the specimen in the time domain. Figure 5 shows the strain and strain rate histories of the polybutadiene rubber specimen. By eliminating time t through Eqs. (22) to (24), we can determine the stress-strain and strain rate-strain relations, which are shown in Fig. 6. The dynamic stress-strain loop is completely closed. The strain rate does

Table 2 Specifications for viscoelastic SHPB system

Material	Striker bar (mm)		Input and output bars (mm)			
	Diameter	Length	Diameter	Length	Distance between strain gage ① and interface A 1 1	Distance between strain gage ② and interface B 1 2
Polymethyl methacrylate (PMMA)	10.0	40	15.0	700	300	50

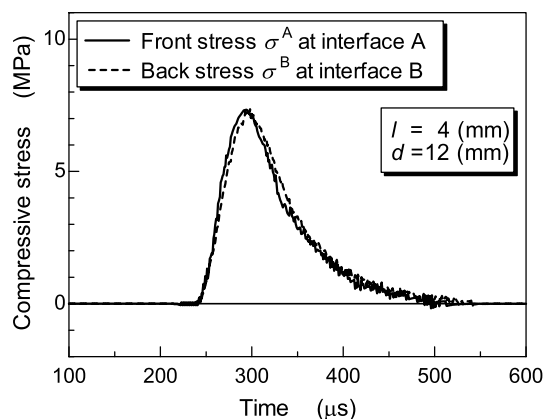


Fig. 4 Compressive stress histories applied at both ends of polybutadiene rubber specimen

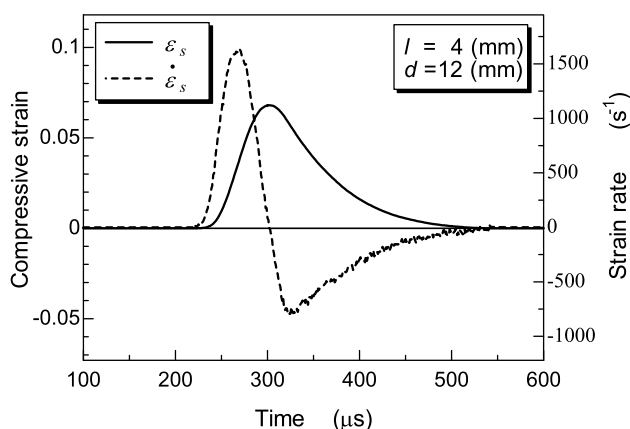


Fig. 5 Compressive strain and strain rate histories for polybutadiene rubber specimen

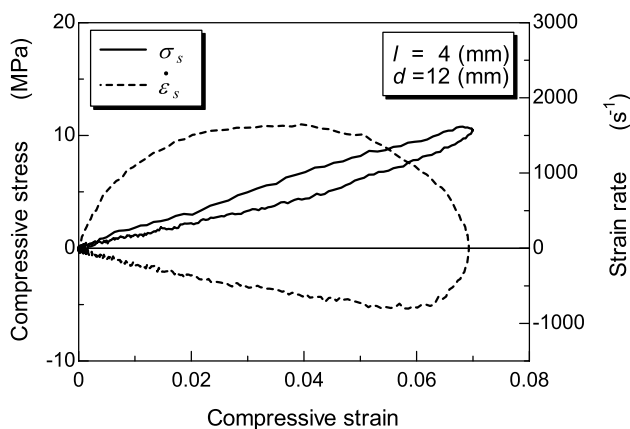


Fig. 6 Compressive stress–strain and strain rate–strain loops for polybutadiene rubber specimen

not remain constant during loading or unloading and varies its sign from compression (+) to tension (–) at a maximum loading strain.

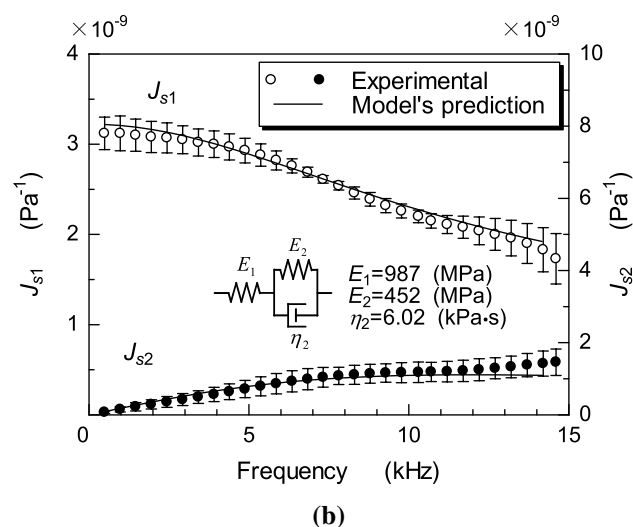
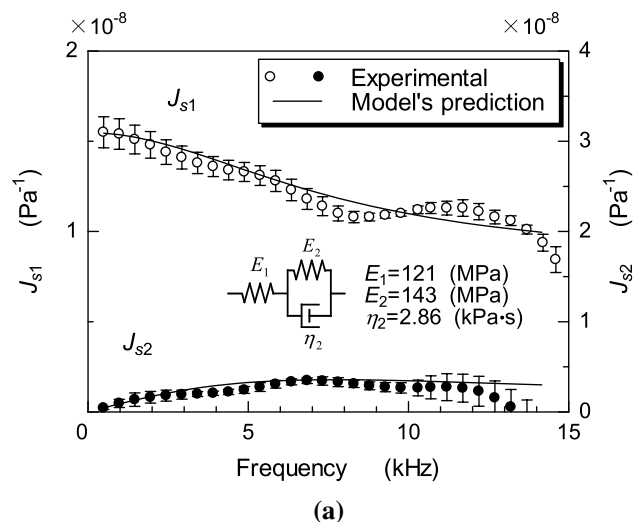


Fig. 7 Frequency dependence of complex compliances of two-piece golf ball materials and identified viscoelastic parameters.

Identification of Mechanical Models

Using Eqs. (22) and (24), we can determine the complex compliance $J_s(\omega)$ of the specimen, which is given by

$$J_s(\omega) = J_{s1}(\omega) - iJ_{s2}(\omega) = \bar{\epsilon}_s(\omega)/\bar{\sigma}_s(\omega). \quad (25)$$

Figure 7 depicts the experimental and predicted complex compliances for the two golf ball materials. The plots denote average values of $J_{s1}(\omega)$ and $J_{s2}(\omega)$ obtained from 10 viscoelastic SHPB tests. Vertical bars on the two curves indicate the standard deviations of the measured $J_{s1}(\omega)$ and $J_{s2}(\omega)$ values. The three viscoelastic parameters (E_1 , E_2 , η_2) were determined using best fits with the plots, and are denoted with solid lines in Fig. 7a, b. As is the case with PMMA, the complex compliances of both the polybutadiene rubber and the ionomer resin can be well approximated

with the three-element solid model up to a frequency of nearly 15 kHz. We can see that the three-element solid models provide reasonable estimations for the dynamic behavior of the golf ball materials.

Validation of Mechanical Models and FE Simulations

Golf Ball Collision Tests

To verify the accuracy of the mechanical models of the two golf ball materials, we performed axial collision tests and measured both contact force histories and coefficients of restitution. Figure 8 shows a schematic of the experimental device for producing axial collisions of the two-piece golf ball with a long elastic bar. The golf ball was mounted on a Nylon 66 sabot and was fired with compressed air through a gun barrel and impinged on one end of a 3000 mm long Ti-6Al-4V alloy bar with a 27 mm diameter. The Nylon 66 sabot (diameter = 50 ± 0.05 mm and length = 40 mm) was stopped by a steel-ring stopper attached to the muzzle of the gun barrel. The generated compressive strain pulse $\epsilon(t)$ was recorded with a pair of P-type semiconductor strain gages (Kyowa, KSP-2-120-E4, gage factor 120) placed at a distance of 250 mm from the impact end of the Ti-alloy bar. The contact force history was then determined from $A E \epsilon(t)$ (A is the cross-sectional area and E is the Young's modulus of the Ti-alloy bar) using elementary one-dimensional wave theory. The incident and rebound velocities, V_i and V_r , of the golf ball were measured with a photo-sensor installed just before the impact end of the Ti-alloy bar. The coefficients of restitution were determined from $-V_r/V_i$ because the mass of the Ti-alloy bar was by far larger than that of the

golf ball. Five measurements of the coefficients of restitution were made at three different incident velocities between 31 and 51 m/s.

Finite Element (FE) Analysis

FE investigations on the axial collision between the two-piece golf ball and the Ti-alloy bar were performed using LS-DYNA code. Figure 9 illustrates the golf ball collision with the Ti-alloy bar and three points in the core region at which axial strain rates were estimated from FE analysis. Figure 10 indicates the construction and dimensions of the two-piece golf ball consisting of the inner and outer materials. Its average weight was 43.4 g. The core and cover parts of the two-piece golf ball were modeled using 8-node solid elements. The Ti-alloy bar was also modeled with the same element types. The numbers of elements used for modeling the core region, the cover region, and the Ti-alloy bar were 12,480, 3744, and 16,800, respectively. The friction between the golf ball

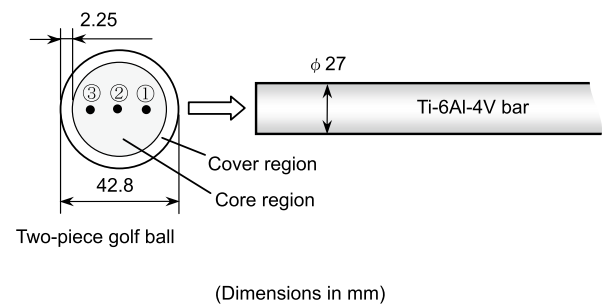
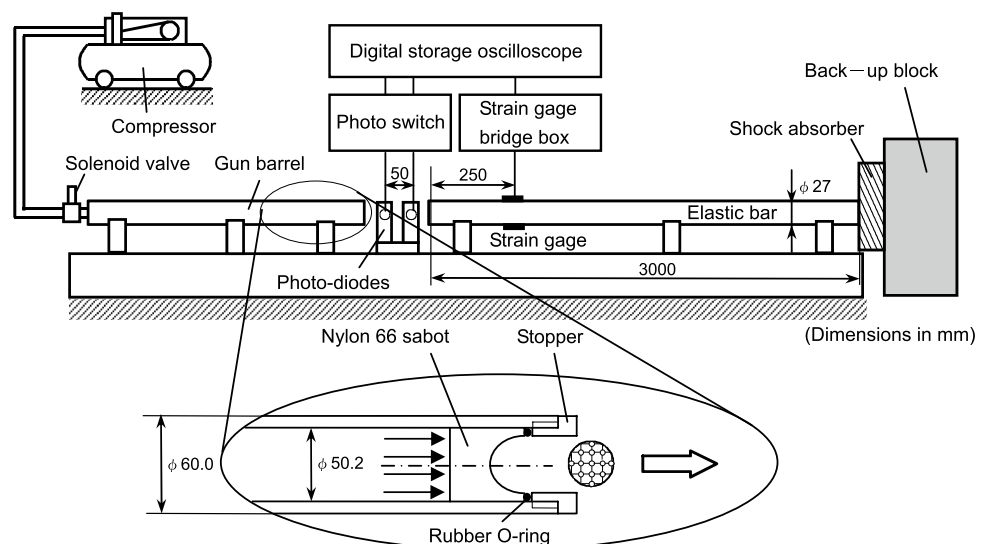


Fig. 9 Illustration of collision between two-piece golf ball and elastic bar and three locations in core region at which strain rates were evaluated using FE simulations

Fig. 8 Schematic of golf ball launching device and measurement system



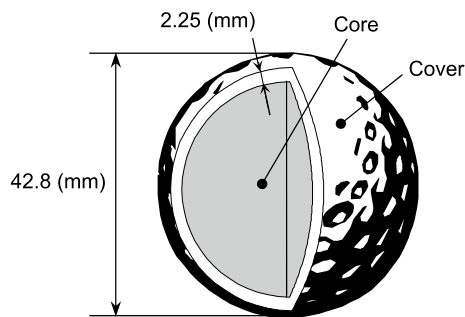


Fig. 10 Construction and dimensions of two-piece golf ball (Windy 384, Kasco, Japan)

and the Ti-alloy bar was assumed to follow Coulomb's friction law. Namely, the coefficient of friction was set to 0.3, which was adopted by Tanaka et al. [36] in numerical simulations of golf ball collisions with a steel bar using FE code in ABAQUS/Explicit. In this work, the explicit central difference scheme was used to integrate the equations of motion with respect to time. The time increment used was $\Delta t = 0.245 \mu\text{s}$. Table 3 lists the mechanical and physical properties of the two golf ball materials and the Ti-alloy bar used in the FE analysis. Figure 11 shows the FE simulation results for the axial stress distribution in the golf ball and the Ti-alloy bar at the maximum deformation at $V_i = 40.3 \text{ m/s}$. The color contour map indicates the components of the normal stress in the axial direction of the bar. Figure 12 exhibits the FE simulation results of the axial strain rate histories at the center of core region ② and at two symmetric points ① and ③, both of which were 10 mm from the center point. The maximum axial strain rates at the three points were estimated to be around $1500\text{--}4000 \text{ s}^{-1}$, corresponding to the same order of strain rates as that for the rubber specimen shown in Fig. 5.

Figure 13 shows the FE simulation results of the effect of the friction coefficient on the contact force histories generated by golf ball collisions with the Ti-alloy bar at $V_i = 31.1 \text{ m/s}$. The friction coefficients ranged from 0.0 to 0.3 and the contact forces were obtained by integrating the stress distributions of the impact face over the cross-section

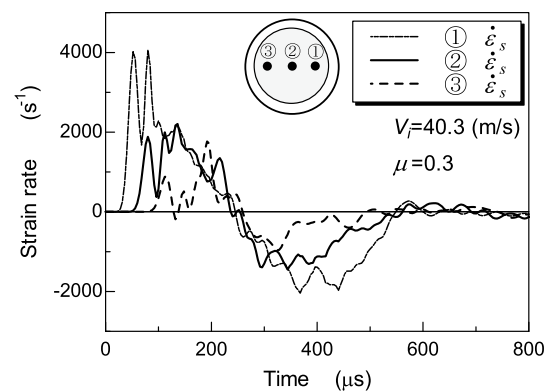


Fig. 12 FE simulation results for axial strain rate histories at different three locations in the core region. (Note: strain rate in compression is positive)

of the Ti-alloy bar. The differences in the contact force histories at any time were very small, and similar results (not shown here) were also obtained for $V_i = 40.3$ and $V_i = 51.0 \text{ m/s}$. The simulation results suggest that the peak of contact forces became slightly larger and the duration became slightly shorter as the friction coefficient increased. Variations in the friction coefficient did not greatly affect the contact force histories. This implies that the contact force histories are dominantly governed by the dynamic properties of the golf ball materials.

Figure 14 shows comparisons between the experimental and numerical results of the contact force histories at three different incident velocities of the golf ball. The experimental and numerical results for $V_i = 31.1$ and $V_i = 40.3 \text{ m/s}$ agree well with each other. In contrast, a slight discrepancy between them is observed at $V_i = 51.0 \text{ m/s}$. This is mainly because non-linear viscoelastic behavior becomes significant with increasing incident velocity and increasing deformation of the golf ball.

Figure 15 shows a comparison of the experimental and predicted relationship between the coefficient of restitution and the incident velocity for the axial collision tests. The solid circles (●) denote the mean values of five experimental data sets, and the open triangles (Δ) indicate predicted values at a coefficient of friction of $\mu = 0.30$. The predicted

Fig. 11 FE mesh and simulation results for axial stress distributions of the golf ball and elastic bar at the maximum deformation of the golf ball at an incident ball speed of 40 m/s (Note: time t is measured from the moment at which the ball contacts the elastic bar)

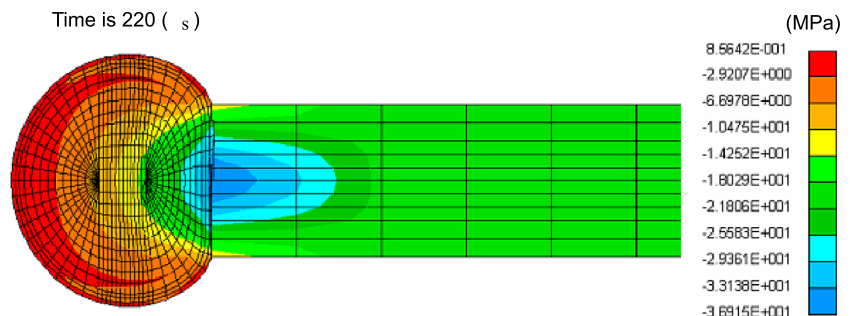


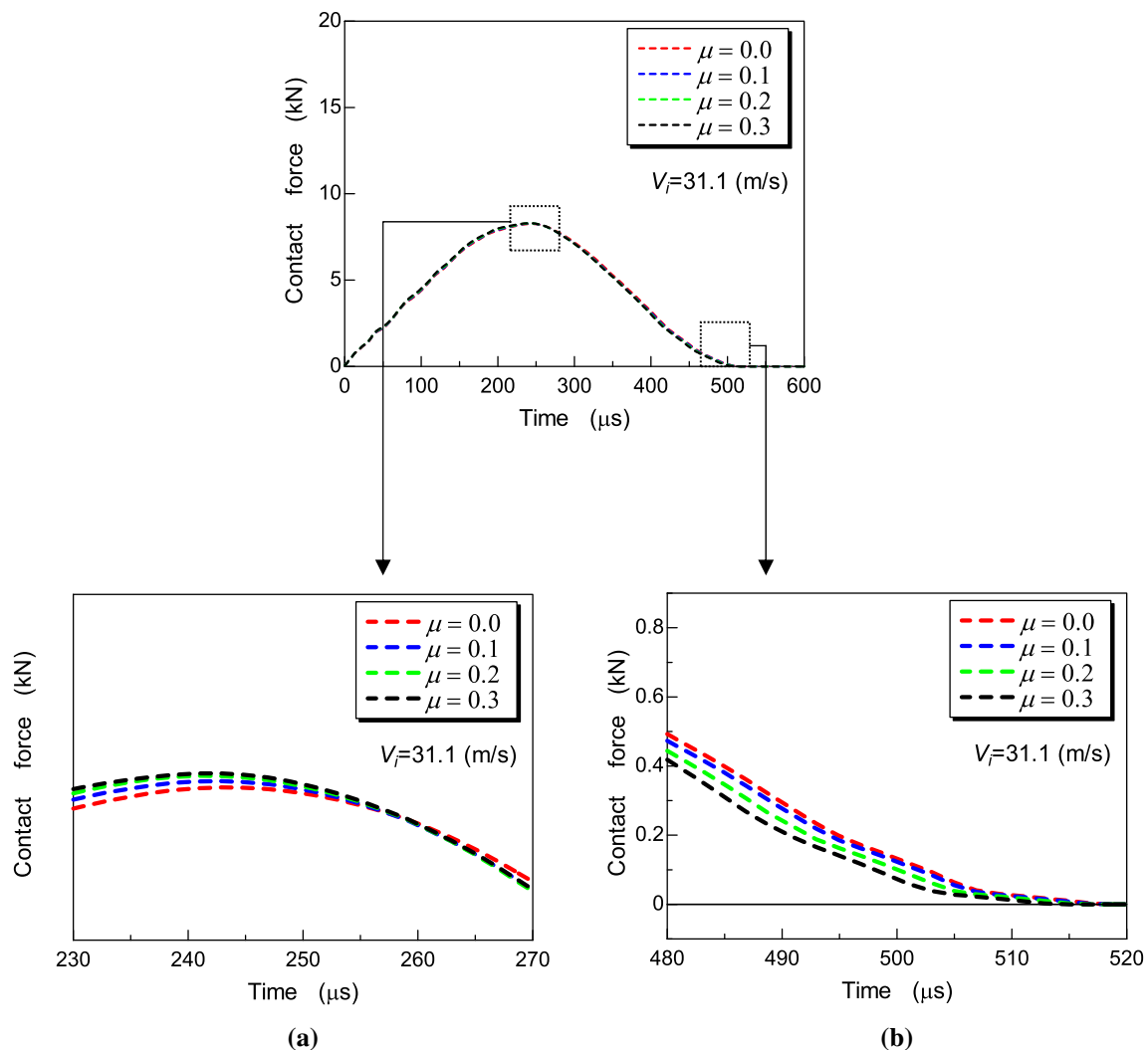
Table 3 Mechanical and physical properties of golf ball materials and elastic bar at room temperature used in FE analysis

Mechanical property	Golf ball (Windy 384)		Elastic bar (Ti-6Al-4V)
	Core (Polybutadiene)	Cover (Ionomer)	
Mass density (kg/m^3)	1140	960	4420
Poisson's ratio	0.376	0.319	0.330
Young's modulus (MPa)	(65.5) ^a	(310) ^a	113,000
E_1 (MPa)	121	987	–
E_2 (MPa)	143	452	–
η_2 (kPa·s)	2.86	6.02	–

^aYoung's modulus is not directly measured and estimated from $E = E_1 E_2 / (E_1 + E_2)$

where E_1 and E_2 are given in this Table

coefficients of restitution agree with the experimental ones, except at $V_i = 51.0$ m/s. The measured and predicted coefficients of restitution were found to decrease with increasing incident velocity. This is because the energy dissipation involved in the deformation process of the golf ball increases with increasing incident velocity. The discrepancies in the coefficients of restitution are closely associated with those in the measured and numerical contact force histories at $V_i = 51.0$ m/s, as shown in Fig. 14. Consequently, the three-element solid models given in Fig. 7 are valid over a strain rate range of up to nearly 4000 s^{-1} with small deformations.

**Fig. 13** FE simulation results for the effect of the friction coefficient on the contact force histories resulting from two-piece golf ball impact at $V_i = 31.1$ m/s.

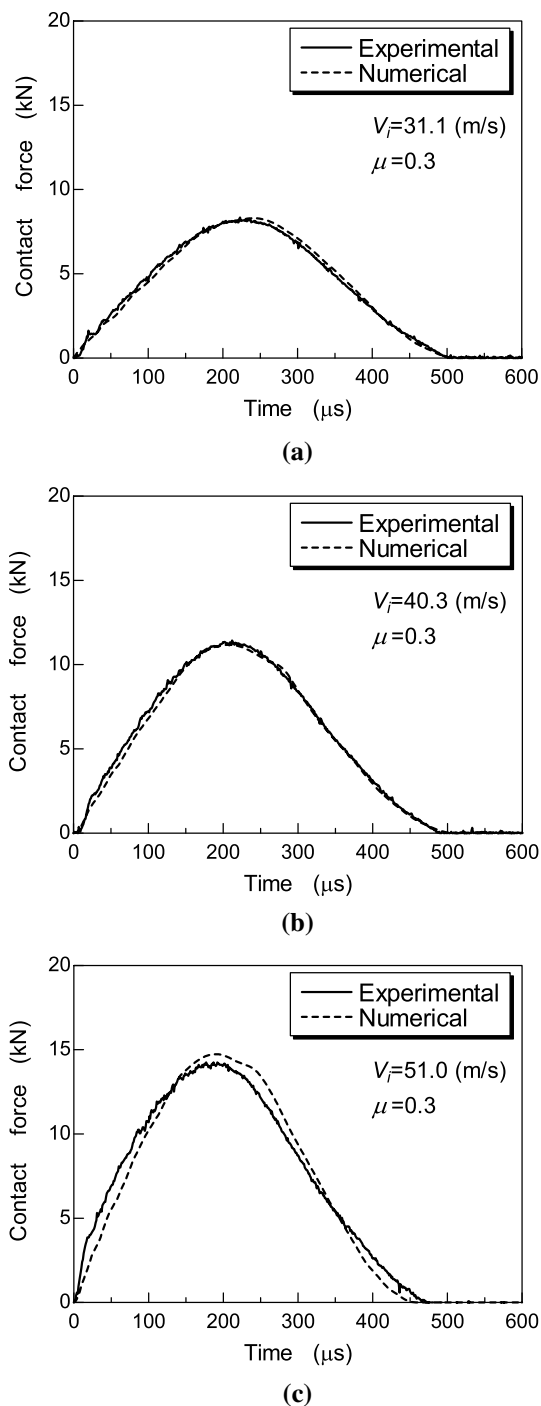


Fig. 14 Experimental and numerical results for contact force histories resulting from two-piece golf ball impact at three different incident velocities

Summary and Conclusions

A viscoelastic split Hopkinson bar made of PMMA bars was developed and applied to evaluate the dynamic stress–strain properties of two-piece golf ball materials. Mechanical

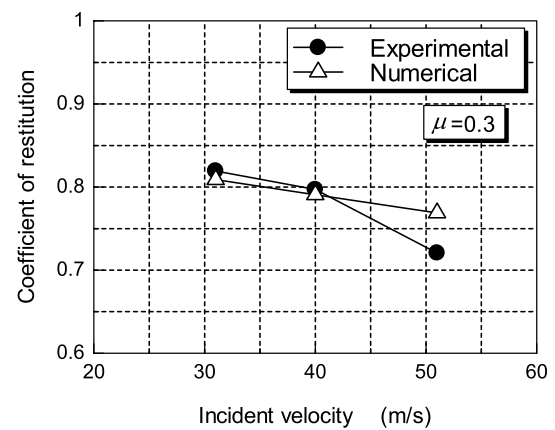


Fig. 15 Experimental and predicted relationship between the coefficient of restitution of a two-piece golf ball and the incident velocity

models for the core and cover materials were identified from the complex compliances derived from the Fourier transforms of three strain pulses. The accuracy of the three-element solid models was verified through comparisons between the experimental and numerical contact force histories during golf ball impacts. The limitations of the three-element solid models were discussed. From the present work, we can draw the following conclusions:

1. The three-element solid model is suitable for describing the viscoelastic behavior of PMMA within a frequency range of up to nearly 15 kHz.
2. The three-element solid models for the core and cover materials identified with the viscoelastic SHPB technique provide reasonable predictions of compressive behavior at strain rates of up to around 4000 s^{-1} within small strains of up to nearly 0.1.
3. As for low-impedance or soft materials, specimens with slenderness ratios that are much less than 0.5 must be used in the viscoelastic SHPB tests to facilitate dynamic stress equilibrium.
4. FE simulations of the golf ball collisions suggest that as the friction coefficient grows, the time to reach a peak in the contact force history shortens and its duration decreases in normal impacts.

Acknowledgements The authors wish to thank two reviewers for their heSSlful comments and suggestions during the preparation of this manuscript.

Appendix

Identification of Mechanical Models for the PMMA Bar

The viscoelastic behavior of the PMMA bar used in the SHPB tests was characterized at room temperature with

the wave propagation method proposed by Sogabe and Tsuzuki [37]. Figure 16 shows a schematic of the longitudinal wave propagation experiment with a 2000 mm long PMMA bar measuring 20 mm in diameter. The mass density was 1180 kg/m^3 . A 100 mm long PMMA striker bar measuring 15 mm in diameter was launched with compressed air from an air compressor and impacted the front end of a PMMA bar supported with V-blocks. Four foil strain gages with a gage length of 1 mm (Kyowa, KFG-1-120-C1-11, gage factor 2.1) were mounted in intervals of 200 mm along the PMMA bar. A pair of strain gages located diametrically opposite on the bar at each position were connected in series to cancel bending waves. The first measurement point x_1 was located at a distance of 100 mm from the impact end. The output signals from the strain gages were fed through a bridge circuit into a digital storage oscilloscope (Iwatsu Electric Co., Model LT-224) and were converted to digital data. The velocities of the striker bar were adjusted so that the peak value of the strain pulse at the first measurement point x_1 was nearly 1000–3000 $\mu\epsilon$. Figure 17 shows typical strain waveforms measured at four different positions along the PMMA bar. The four measured strain waves were resolved into their Fourier components by employing fast Fourier transforms with respect to time t . Fig. 18 depicts the absolute values of Fourier components, or the Fourier spectrums of the four strain pulses. A little attenuation of the amplitudes can be observed over a given frequency range of 15 kHz. The spectrums $\bar{\epsilon}_j(\omega) (j = 1 - 4)$ have almost similar peak amplitudes of nearly $4 \times 10^{-8} \text{ s}$ at a zero frequency, corresponding to the area within each waveform in Fig. 17. We found that these waveforms propagate, keeping the area constant. When the assumption of $a/\Lambda < 0.1$ [38] (a is the bar radius and Λ is the wavelength) is satisfied, the longitudinal motion of the bar can be regarded as one-dimensional. The maximum of the frequency components included in the strain waveforms of these experiments was nearly 10 kHz. The wave front velocity C_f in Fig. 17 was estimated to be approximately 2200 m/s from the strain wave propagation time. Then, $a/\Lambda = a \cdot f / C_f \cong 0.045$, indicating that the

geometric dispersion was negligibly small. From Eq. (8), we can obtain the following solutions from the Fourier transforms of strain histories:

$$\bar{\epsilon}_j(x, \omega) = \bar{\epsilon}_0(0, \omega) \cdot \exp[-\{\alpha(\omega) + ik(\omega)x_j\}] ; j = 1, 2, \dots, n. \quad (\text{A1})$$

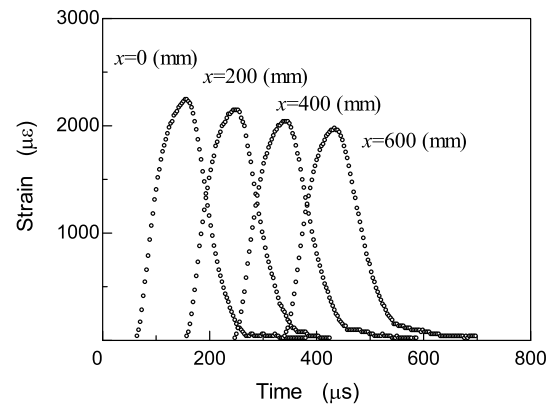


Fig. 17 Typical strain waveforms measured at four different locations along a PMMA bar revealing attenuation

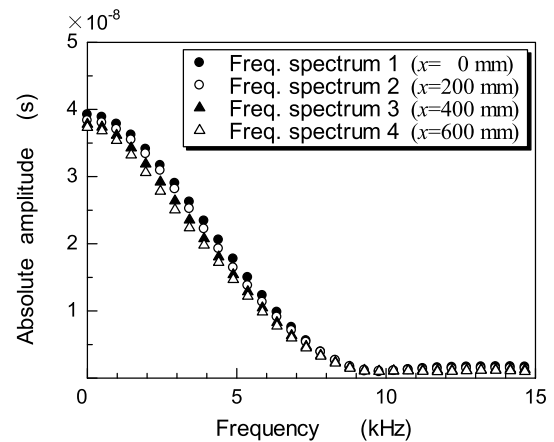
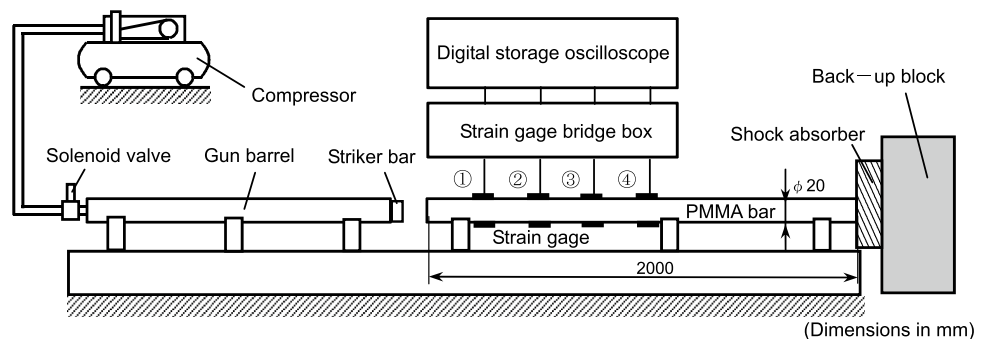


Fig. 18 Fourier spectrums of four measured strain waveforms in a PMMA bar

Fig. 16 Schematic of longitudinal wave propagation experiment in a PMMA bar



$\alpha(\omega)$ and $k(\omega)$ can be determined by applying a least-squares method to Eq. (A1).

$$\left. \begin{aligned} \alpha(\omega) &= \frac{\sum x_j \sum \log |\bar{\epsilon}_j(\omega)| - n \sum x_j \log |\bar{\epsilon}_j(\omega)|}{n \sum x_j^2 - (\sum x_j)^2} \\ k(\omega) &= \frac{\sum x_j \sum \arg \bar{\epsilon}_j(\omega) - n \sum x_j \arg \bar{\epsilon}_j(\omega)}{n \sum x_j^2 - (\sum x_j)^2} \end{aligned} \right\} \quad (\text{A2})$$

in which $n (=4)$ is the number of measurement points and $\arg = \tan^{-1} \{J_2(\omega)/J_1(\omega)\}$ denotes the phase angle of $\bar{\epsilon}_j(\omega)$. From Eq. (9), we can experimentally determine the real and imaginary parts of the complex compliance as functions of ω , or $J_1(\omega)$ and $J_2(\omega)$. Fig. 19 shows the plots for average values of $J_1(\omega)$ and $J_2(\omega)$ obtained from 10 wave propagation experiments. The respective vertical bars on the two curves indicate standard deviations for $J_1(\omega)$ and $J_2(\omega)$. In an effort to adopt an appropriate mechanical model for the complex compliances, we investigated the frequency dependences of $J_1(\omega)$ and $J_2(\omega)$ for a three-element solid model (Fig. 20a) and a four-element fluid model (Fig. 20b). The analytical expressions for $J_1(\omega)$ and $J_2(\omega)$ for each model are given respectively by

$$\left. \begin{aligned} J_1(\omega) &= \frac{1}{E_1} + \frac{E_2}{E_2^2 + (\omega\eta_2)^2} \\ J_2(\omega) &= \frac{\omega\eta_2}{E_2^2 + (\omega\eta_2)^2} \end{aligned} \right\} \quad (\text{A3})$$

for the three – element solid model and

$$\left. \begin{aligned} J_1(\omega) &= \frac{1}{E_1} + \frac{E_3}{E_3^2 + (\omega\eta_3)^2} \\ J_2(\omega) &= \frac{1}{\omega\eta_2} + \frac{\omega\eta_3}{E_3^2 + (\omega\eta_3)^2} \end{aligned} \right\} \text{ for the four – element fluid model.} \quad (\text{A4})$$

Both of these are shown graphically in Fig. 20. Figure 19 indicates that $J_1(\omega)$ decreases up to a frequency of around 4 kHz, and then become almost constant, while

$J_2(\omega)$ reaches a peak at about 4 kHz, and then decreases gradually. It follows that the three-element solid model shown in Fig. 20a can be selected as a valid model exhibiting such characteristics. The three viscoelastic parameters (E_1 , E_2 , and η_2) were determined from best fits to the plots, and are included in Fig. 19. Three strain waveforms $\epsilon_2(t)$, $\epsilon_3(t)$, and $\epsilon_4(t)$ can be obtained by applying the inverse Fourier transform to Eq. (A1) using the experimental waveform $\epsilon_1(t)$ at $x = 0.0$ m. Fig. 21 provides a comparison between the three measured and predicted strain waveforms, indicating good agreement. The three viscoelastic parameters for mechanical models of the input and output bars of PMMA were used in the viscoelastic SHPB tests.

For reference, the viscoelastic parameters identified for the three-element solid model of PMMA are compared with those given in Refs [23, 25, 37] in Table 4. The values of the three parameters are in reasonably good agreement with those obtained by others. Slight variations in the respective parameters are probably due to different manufacturing processes for PMMA bars.

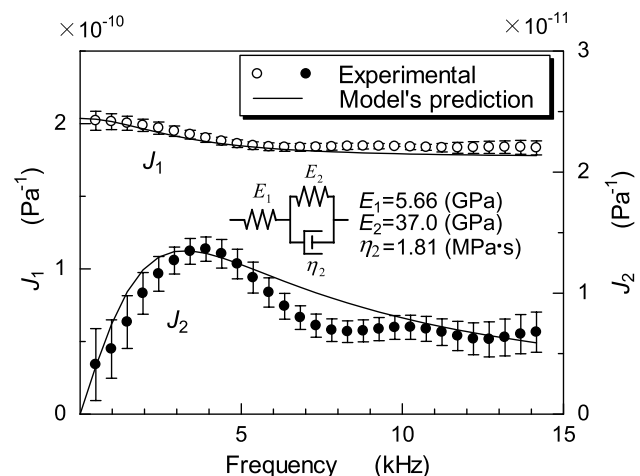


Fig. 19 Frequency dependence of complex compliance of PMMA

Table 4 Comparison of viscoelastic parameters identified for three-element solid model of PMMA at room temperature

Reference	Viscoelastic parameter			Poisson's ratio ν	Mass density $\rho(\text{kg/m}^3)$
	E_1 (GPa)	E_2 (GPa)	η_2 (MPa.s)		
Present work	5.66	37.0	1.81	0.360	1180
Sogabe & Tsuzuki [37]	5.25	16.9	2.13	0.365	1183
Bussac et al. [23]	5.78	72.3	4.75	(–) ^a	1183
Ahonsi et al. [25]	5.99	28.5	0.68	0.38	1190

Values of viscoelastic parameter given for PMMA are converted from those for three-element standard linear solid model

^a(–) indicates no data available

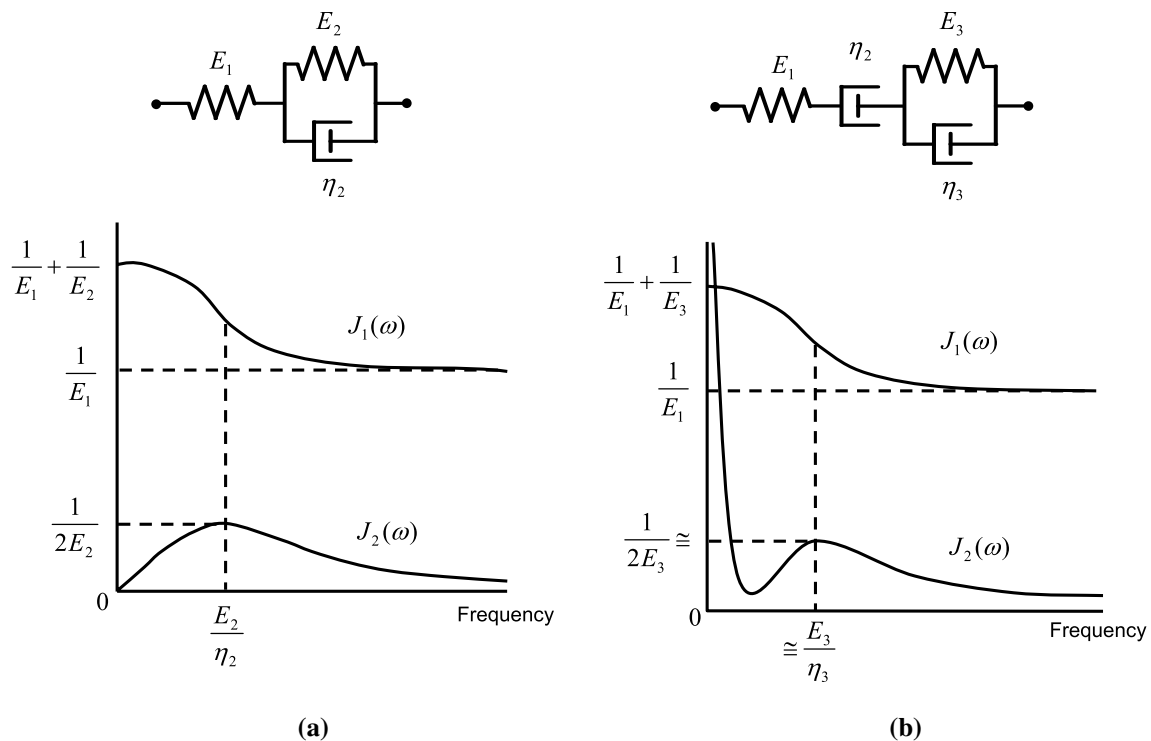


Fig. 20 Frequency dependence of real and imaginary parts of complex compliances, $J_1(\omega)$ and $J_2(\omega)$, for two different mechanical models

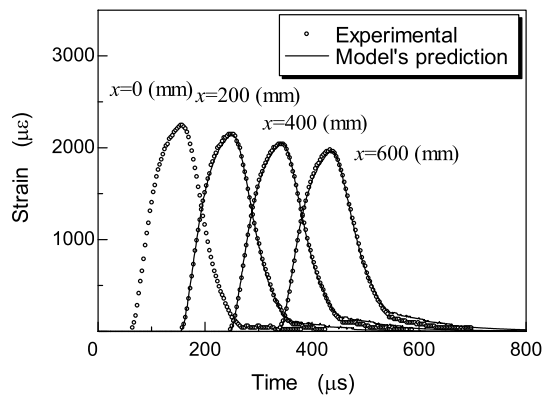


Fig. 21 Comparison between measured and predicted strain wave-forms at three different locations along PMMA bar

References

- Kolsky H (1949) An investigation of mechanical properties of materials at very high rates of loading. *Proc Phys Soc Lond B* 62(11):676–700
- Wang L, Labibes K, Azari Z, Pluvinage G (1994) Generalization of split Hopkinson bar technique to use viscoelastic bars. *Int J Impact Eng* 15(5):669–686
- Aleyaasin M, Harrigan JJ (2010) Wave dispersion and attenuation in viscoelastic polymeric bars: analysing the effect of lateral inertia. *Int J Mech Sci* 52(5):754–757
- Zhao H, Gary G (1995) A three dimensional analytical solution of the longitudinal wave propagation in an infinite linear viscoelastic cylindrical bar. Application to experimental techniques. *J Mech Phys Solids* 43(8):1335–1348
- Sogabe Y, Yokoyama T, Yokoyama T, Nakano M, Kishida K (1995) A split Hopkinson bar method for testing materials with low characteristic impedance. *ASME Dynamic Fracture, Failure and Deformation PVP 300* (editors: Nishioka T, Epstein JS):137–143
- Zhao H, Gary G, Klepaczko JR (1997) On the use of a viscoelastic split Hopkinson pressure bar. *Int J Impact Eng* 19(4):319–330
- Zhao H (1997) Testing of polymeric foams at high and medium strain rates. *Polymer Test* 16(5):507–516
- Zhao H, Gary G (1997) An experimental investigation of compressive failure strength of fibre-reinforced polymer-matrix composite plates under impact loading. *Compos Sci Tech* 57(3):287–292
- Zhao H, Gary G (1998) Crushing behaviour of aluminium honeycombs under impact loading. *Int J Impact Eng* 21(10):827–836
- Zhao H, Gary G (1997) A new method for the separation of waves: application to the SHPB technique for an unlimited duration of measurement. *J Mech Phys Solids* 45(7):1185–1202
- Bacon C (1998) An experimental method for considering dispersion and attenuation in a viscoelastic Hopkinson bar. *Exp Mech* 38(4):242–249
- Bacon C (1999) Separation of waves propagating in an elastic or viscoelastic Hopkinson pressure bar with three-dimensional effects. *Int J Impact Eng* 22(1):55–69
- Bacon C, Brun A (2000) Methodology for a Hopkinson test with a non-uniform viscoelastic bar. *Int J Impact Eng* 24(3):219–230
- Sawas O, Brar NS, Brockman RA (1998) Dynamic characterization of compliant materials using an all-polymeric split Hopkinson bar. *Exp Mech* 38(3):204–210

15. Cheng ZQ, Crandall JR., Pilkey WD (1998) Wave dispersion and attenuation in viscoelastic split Hopkinson pressure bar. *Shock Vib* 5(5–6):307–315
16. Bussac MN, Collet P, Gary G, Othman R (2002) An optimisation method for separating and rebuilding one-dimensional dispersive waves from multi-point measurements. Application to elastic or viscoelastic bars. *J Mech Phys Solids* 50(2):321–349
17. Casem DT, Fournery WL, Chang P (2003) Wave separation in viscoelastic pressure bars using single-point measurements of strain and velocity. *Polymer Test* 22(2):155–164
18. Casem DT, Fournery WL, Chang P (2003) A polymeric split Hopkinson pressure bar instrumented with velocity gages. *Exp Mech* 43(4):420–427
19. Mousavi S, Welch K, Valdek U, Lundberg B (2005) Non-equilibrium split Hopkinson pressure bar procedure for non-parametric identification of complex modulus. *Int J Impact Eng* 31(9):1133–1151
20. Liu Q, Subhash G (2006) Characterization of viscoelastic properties of polymer bar using iterative deconvolution in the time domain. *Mech Mater* 38(12):1105–1117
21. Doman DA, Cronin DS, Salisbury CP (2006) Characterization of polyurethane rubber at high deformation rates. *Exp Mech* 46(3):367–376
22. Quellet S, Cronin D, Worswick M (2006) Compressive response of polymeric foams under quasi-static, medium and high strain rate conditions. *Polymer Test* 25(6):731–743
23. Bussac MN, Collet P, Gary G, Lundberg B, Mousavi S (2008) Viscoelastic impact between a cylindrical striker and a long cylindrical bar. *Int J Impact Eng* 35(4):226–239
24. Salisbury CP, Cronin DS (2009) Mechanical properties of ballistic gelatin at high deformation rates. *Exp Mech* 49(6):829–840
25. Ahonsi B, Harrigan JJ, Aleyaasin M (2012) On the propagation coefficient of longitudinal stress waves in viscoelastic bars. *Int J Impact Eng* 45:39–51
26. Butt HSU, Xue P (2014) Determination of the wave propagation coefficient of viscoelastic SHPB: significance for characterization of cellular materials. *Int J Impact Eng* 74:83–91
27. Harrigan JJ, Ahonsi B, Palamidi E, Reid SR (2014) Experimental and numerical investigations on the use of polymer Hopkinson pressure bars. *Phil Trans R Soc A* 372:20130201
28. Butt HSU, Xue P, Jiang TZ, Wang B (2015) Parametric identification for material of viscoelastic SHPB from wave propagation data incorporating geometrical effects. *Int J Mech Sci* 91(2023):46–54
29. Johnson TPM, Sarva SS, Socrate S (2010) Comparison of low impedance split-Hopkinson pressure bar techniques in the characterization of polyurea. *Exp Mech* 50(7):931–940
30. Irausquin I, Pérez-Castellanos JL, Miranda V, Teixeira-Dias F (2013) Evaluation of the effect of the strain rate on the compressive response of a closed-cell aluminum foam using the split Hopkinson pressure bar test. *Mater Des* 47:698–705
31. Flügge W (1972) *Viscoelasticity*, Springer, Berlin 2nd revised edition: 21
32. Gray G. T. III (2000) Classic split-Hopkinson pressure bar testing, in *ASM Handbook: Vol. 8, Mechanical Testing and Evaluation*. ASM International, Materials Park, Ohio pp 471
33. Chen W, Zhang B, Forrestal, MJ (1999) A split Hopkinson bar technique for low-impedance materials. *Exp Mech* 39(2):81–85
34. Siviour CR, Walley SM, Proud WG, Field JE (2005) The high strain rate compressive behaviour of polycarbonate and polyvinylidene difluoride. *Polymer* 46(26):12546–12555
35. Gray GT III (2000) Classic split-Hopkinson pressure bar testing, *ASM Handbook Vol. 8, Mechanical Testing and Evaluation*. ASM International. Materials Park, Ohio 2000:465–466
36. Tanaka K, Sato F, Oodaira H, Teranishi Y, Sato F, Ujihashi S (2006) Construction of the finite-element models of golf balls and simulations of their collisions, *Proc I Mech Eng Part L* 220(1):13–22
37. Sogabe Y, Tsuzuki M (1986) Identification of the dynamic properties of linear viscoelastic materials by the wave propagation testing. *Bull JSME* 29(254):2410–2417
38. Kolsky H (1963) *Stress waves in solids*. Dover, New York